WP15ER-PR(18) 19887

F Consoli et al.

Generation of intense quasi-electrostatic fields due to deposition of particles accelerated by petawatt-range laser-matter interactions

Preprint of Paper to be submitted for publication in Scientific Reports

This work has been carried out within the framework of the EUROfusion Consortium and has received funding from the Euratom research and training programme 2014-2018 under grant agreement No 633053. The views and opinions expressed herein do not necessarily reflect those of the European Commission.

Generation of intense quasi-electrostatic fields due to deposition of particles accelerated by petawatt-range laser-matter interactions

F. Consoli[1], R. De Angelis[1], T. Robinson[2], S. Giltrap[2], G. S. Hicks[2], E. J. Ditter[2], O. C. Ettlinger[2], Z. Najmudin[2], M. Notley[3], and R. A. Smith[2]

[1]ENEA – C.R. Frascati, Fusion and Nuclear Safety Department, Via E. Fermi 45, 00044 Frascati, Italy

[2]The Blackett Laboratory, Imperial College London, Prince Consort Road, London, SW7 2AZ, United Kingdom

[3]Central Laser Facility, STFC Rutherford Appleton Laboratory, Chilton, Didcot, Oxon, OX11 0QX, United Kingdom

We demonstrate here for the first time that charge emitted by laser-target interactions at petawatt peak-powers can be efficiently deposited on a capacitor-collector structure and lead to the rapid generation of large quasi-static electric fields over wide (tens-of-centimeters scale-length) regions well-shielded against ionizing plasma radiation, with intensities much higher than common ElectroMagnetic Pulses (EMPs) generated by the same experiment. A good agreement was obtained between measurements from a classical field-probe and calculations based on particle-flux measurements from a Thomson spectrometer. Proof-of-principle particle-in-cell simulations reproduced the measurements of field evolution in time, giving a useful insight into the charging process, generation and distribution of fields. The understanding of this charging phenomenon and of the related intense fields is very important for present and future facilities studying laser-plasma-acceleration and inertial-confinement-fusion, but also for application to the conditioning of accelerated charged-particles, the generation of intense electric and magnetic fields and many other multidisciplinary high-power laser-driven processes.

The generation of particle beams due to the interaction of energetic, high-intensity, short-pulse lasers with a target is currently an important topic of research[1] with the potential to underpin future table-top and high-peak current particle accelerators. There are however current limitations to the use of these high-flux sources for potential applications, particularly due to their intrinsic broad-energy spectrum and energy-dependent spatial divergence. Thus, many investigations have been focused on overcoming these constraints[1-9] with the aim of increasing the range of possible applications of laser-driven accelerators to radiography[10,11], oncology[12,13], medical imaging[14], astrophysics[15,16], high-energy-density-physics[17,18] and ion-beam fast-ignition in the frame of inertial confinement fusion[19]. In addition, the large charge-separation induced over a few picosecond timescale in these experiments can be very interesting for uses quite different and distinct from classical particle beam - target schemes. Tailored large-amplitude electric and magnetic fields can also be efficiently created in this way[2,6,9,20-24]. When high intensity lasers are applied to a target, electrons are accelerated first, typically to relativistic energies[1,25,26]. If the interaction is on the surface of a suitable hollow-cylinder target, an ultrafast laser-driven electrostatic micro-lens can be created, with very high transient radial *electric fields*, capable of focusing and energy-selecting MeV-range proton beams produced by an accelerator placed nearby, either one of classical type or one based on laser-matter interactions[2,6]. Alternatively, very strong quasi-static *magnetic fields* can be generated from the interaction of lasers with spiral targets[24] or target-coil geometries[20-23,27], and used for similar purposes. Once fast electrons leave the target, they are followed later in time by much slower laser-accelerated ions. An overall positive charge is thus present on the target for relatively large times[25,26,28,29]. In a conductive target setup, intense transient currents are spontaneously created as a result; they act to neutralize this charge, and are capable of driving powerful electromagnetic waves[9,28-32]. The transient fields generated by such charge-waves can be very effective for collimation and post-acceleration of laser-driven ion beams, for example in coil-shaped targets[9]. On the other hand, these transient currents are also known to be one of the main sources of intense

ElectroMagnetic Pulse (*EMP*) generation in the radiofrequency-microwave range[28,29,32], whose field is capable of degrading data capture or damaging electronic equipment close to the experimental chamber. In all these cases, the region where the generated fields have maximum intensity is mainly localized on a rather small volume around the laser interaction-point on the target, which is thus also heavily affected by ionizing electromagnetic (UV, X and γ rays) and particle radiation coming from the laser-plasma. Although there is now a strong interest in studying and employing these schemes of electric and magnetic field generation, one of the associated well-known problems is the difficulty of performing reliable and accurate field measurements[2,20,21], since the local environment of a laser-matter interaction (with high particle and radiation fluxes, strong shocks and plasma flow) places severe limitations. These extreme conditions are also a considerable challenge for many proposed applications of these electromagnetic fields[2,6,9,20-24,33] and this will be an increasing problem in the future with the advent of higher repetition rate laser drivers.

In this work we show for the first time that the charge emitted by an intense laser-target interaction can be efficiently deposited onto one plate of an open capacitor-collector structure (see the basic scheme of Figure 1) and can thus be used for the fast generation of very large quasi-static electric fields. These fields can be easily obtained in regions having large spatial extent and can be very well shielded against direct ionizing radiation produced by the powerful laser-matter interaction. Simple evolutions from the basic scheme shown in Figure 1, can also readily lead to more complex structures where specific electric field distributions, not necessarily uniform, can be achieved. Due to the extreme laminarity of laser-driven particle flows[1] it is possible to place the collector plate at some distance from the laser interaction-point, while enlarging its transverse dimension to ensure capture of the majority of the particle stream. Increasing the distance in this way has the advantage of reducing the intensity of ionizing electromagnetic radiation from the plasma reaching the collector. Moreover, the collection plate can be made thick enough to provide suitable shielding of the electric-field-area behind it, where

field measurements or applications can be conducted. This is one of the main advantages of this simple setup.

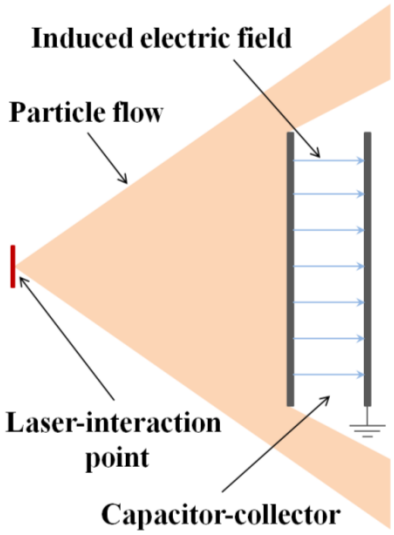

Figure 1. Principle scheme of the field induced due to charge deposition on one plate of a capacitor-collector setup. The system is initiated by an energetic particle flow from a pulsed laser driven source, impulsively creating a large electric field.

Depending on the position, these powerful electric fields can have intensities much higher than the EMPs generated in the same experiment. As shown in this paper, their accurate measurement can be easily performed by classical field-probes, and the schemes for their production can be efficiently run with repetitive high-power lasers. One application of primary importance for them is the efficient focusing, deflection and energy-selection of the charged particle beams emitted by a separate apparatus[34], such as a conventional accelerator or one based on a laser-plasma interaction. The large deposited charge leads to remarkable electric fields and related voltages which are difficult to obtain with a classical power supply in steady-state operation, and with the important characteristic that these fields can be created with short rise-times and at a desired time, absolutely synchronized with the main laser beam. Moreover, very high currents can be generated if the accumulated large charge is then short-circuited to ground by a fast switch. This can be used to drive ultrashort travelling

electromagnetic waves for controlling and optimizing laser-accelerated ions[9], or to generate very high magnetic fields that can be suitable for many different purposes[4,5,8,16,20-24,27,33]. Improvements to particle-acceleration schemes are of immediate interest for the phenomenon described, but the remarkable features of the technique also lends itself to a range of further applications that is very wide and multidisciplinary. In particular, these electric fields of high intensity and wide spatial extent can be directly applicable for biological and medical studies[35], material and device characterization[36-39], electromagnetic-compatibility investigations[38,39] and terahertz generation[40,41].

Results

Experimental measurements. The geometry of the setup used in the experiment is shown in Figure 2a. The laser is focused by an off-axis parabolic mirror onto a thin plastic target with normal incidence. The coordinate system we used to describe the geometry is centered on the laser-target interaction point, with *x*-coordinate normal to target surface. Three Thomson Spectrometers are used to detect particles emitted by means of TNSA process[1] along forward (TS2 and TS3) and backward (TS1) directions with respect to the incoming laser. The focusing parabola consists of 110 mm thick, 650 mm diameter glass substrate with a 620 mm silver front-surface, placed at ~1.8 m distance from target. A D-Dot differential electric-field sensor[43] (see Figure 2b) was placed behind the parabola (as shown in Figure 2a) ensuring good isolation from direct particle and electromagnetic radiation fluxes from the target.

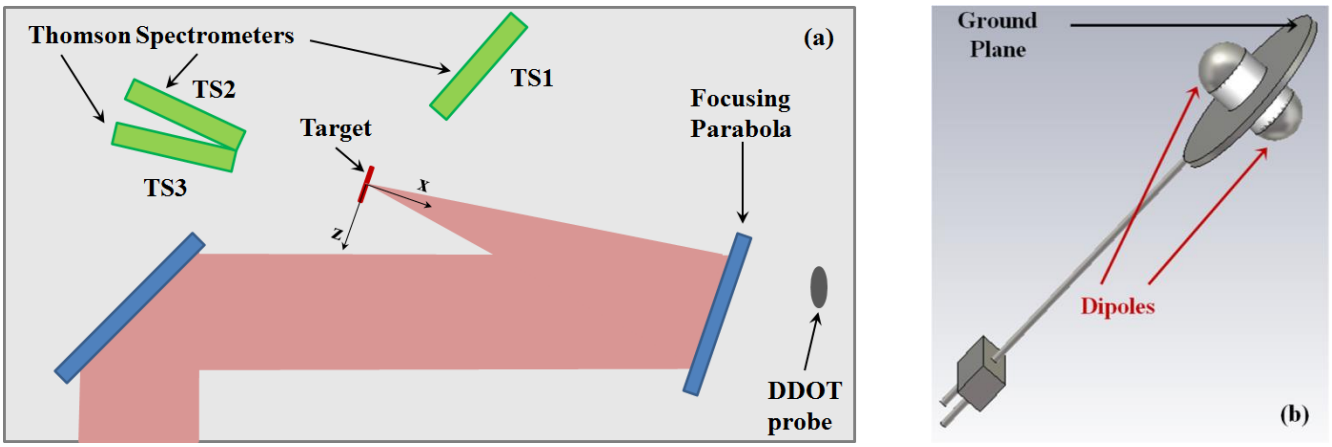

Figure 2. a) Top-view scheme of the vacuum chamber; ~400 J of laser energy (red beam) is brought to a ~6 μm FWHM focal-spot diameter on a thin-foil target using an F/3 off-axis parabola, with the resulting particle flux diagnosed by multiple Thomson ion spectrometers. b) Scheme of the D-DOT probe used, situated behind the parabola and shielded from direct particle and electromagnetic radiation from the target.

A differential signal is generated across the D-Dot probe, proportional to the time-derivative of the incident electric-field component normal to the probe ground-plane. A *balun*[42] was connected to the two probe outputs to convey this signal to a long coaxial cable coupled to a fast oscilloscope. For a 386 J, 1.7 ps laser pulse on target (shot #29, see Table 1 for details) the resulting V_{DDOT} signal is shown in Figure 3a. At first sight, the trace looks like a classical *ElectroMagnetic Pulse* generated by laser-plasma interaction[43-49], with a fast rise followed by an envelope with an exponential decay. We have arbitrarily set the origin of the time-scale at the beginning of the main pulse. The time duration of the signal, with respect to the background electrical noise of the oscilloscope, is ~400 ns. The time-resolved spectrogram[47] of this signal is shown in Figure 3b. It is apparent that a low-frequency component (LFC) is present approximately over the [40,80] ns interval, while the remaining high-frequency component (HFC) has a broad spectrum up to at least 6 GHz.

Through a process of accurate cable frequency-domain deembedding, described in the Methods section, from the V_{DDOT} signal it was possible to recover the actual V_{DDOT-B} produced at the balun output. The component of the applied electric field normal to the D-Dot ground plane can be thus found by time integration of V_{DDOT-B}[42], and is shown for #29 in Figure 3c. The two main components, already identified with the aid of the spectrogram, are here rather clear. In particular, the broadband HFC appears as a modulation with respect to the low-frequency component; it has a maximum peak-peak amplitude of 172 kV/m and gradually decreases with time. This is the classical form of an *EMP* due to a laser-plasma interaction[32,43-49]. Very interesting results are visible for the LFC. A high field increase on the [30,93] ns time interval (named *b* in Figure 3c) is visible: ΔE_n ~600 kV/m, that we were able to detect with good accuracy, as described in detail in the Methods section. There is a noticeable slow decrease of the field intensity over the *d* and *e* intervals. Signal variations are rather low also over intervals *a* and *f*, and comparable with the related measurement accuracy.

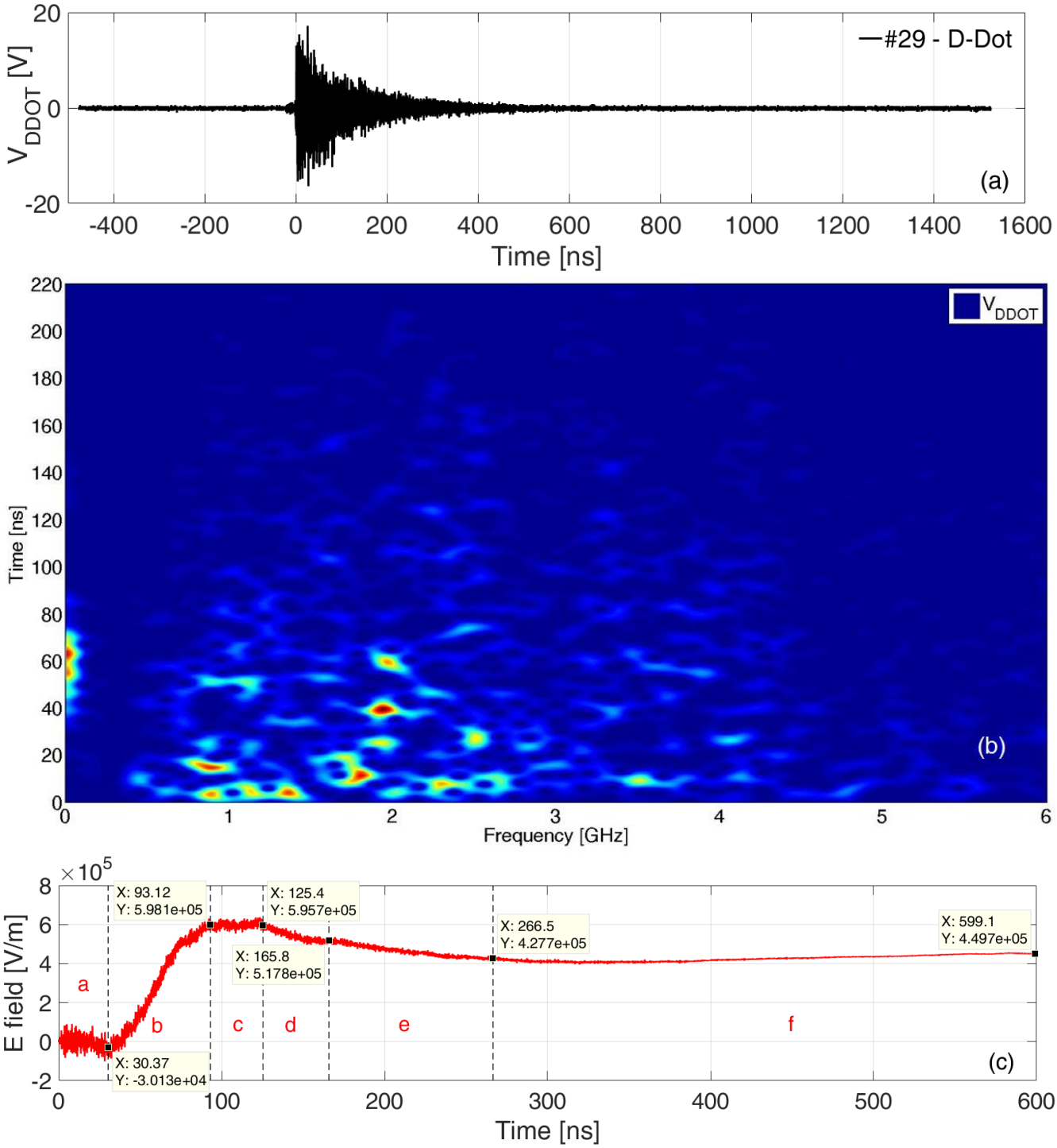

Figure 3. a) V_{DDOT} signal detected by the D-Dot probe in shot #29; b) Time gated spectrogram of the signal; c) recovered component of the electric field normal to the D-Dot ground plane. Time intervals *a-f* identified in (c) are discussed in more detail in the main text.

It is well known from the literature[28,29,32,49,50], and also verified by us in this experiment with a few nanosecond accuracy, that a strong EMP signal is generated at the moment of laser-target interaction, and then reaches the D-Dot probe at light velocity. It is thus evident that the rising of this huge field observed in the *b* interval (Figure 3c), clearly delayed with respect to the moment when the laser hits the target, has to be related to charged particles accelerated by the laser-matter interaction as distinct from prompt EM radiation. In particular, it can be readily associated with charges reaching the silver-coated glass mirror of the focusing parabola and depositing on its surface. The small slopes of the *c, d, e, f* time intervals in Figure 3c suggest that some neutralization of the deposited charge on the parabola then occurs, which might come from either other particles arriving at later times, or charge relaxation-processes with a time constant governed by the parabola structure and holder. This would finally lead to the slow decay to zero of the field.

The laser acceleration mechanism in our experiments lies in the target-normal sheath acceleration (TNSA) regime[1], and under these conditions energetic multi-MeV ions are expected in forward direction (and observed by the Thompson spectrometers TS2 and TS3 shown in Figure 2; a paper is in preparation regarding these results). It is well known that these forward ions are accompanied by particles accelerated in the backward direction (towards the laser) and with a broad angular distribution[1,51-55]**.** In particular, in some conditions of high focal intensities on sub-micrometer targets it has been shown that forward and backward accelerated ions can have roughly comparable energies[51,53,54,55]. If we consider the scheme of a classical time-of-flight detector, from geometrical considerations we can estimate the energy range of possible particles reaching the parabola surface from the extremes of the *b* time-interval in Figure 3: electrons up to keV energy and protons up to MeV energy. In Figure 4a we show the comparison of multiple electric field profiles obtained by D-Dot measurements when shooting with similar laser energy on targets made of the same plastic but of different thicknesses, as detailed in Table 1. Higher fields are generated for targets with smaller

thickness. Indeed, this is also the condition to achieve more accelerated particles and at higher energy[1,51,54,55]. The timing of the rise of the electric field relative to the time of the laser also changes depending on the shot; in particular, for the thinnest target (shot #16) this occurs earlier with respect to the others, as expected for more energetic protons. These considerations are well confirmed by the spectrum of protons detected by the TS1 spectrometer along the backward direction (see Figure 2a), given for #16 and #29 in Figure 4b. In Figure 4c and 4d the same spectra are shown with the associated detection noise-limit. Protons with energies exceeding 10 MeV were detected. Higher energies and larger number of particles are present for #16, corresponding to larger electric-field measurements shown in Figure 4a. The lower energy-threshold of detection for the spectrometer was ~1 MeV, and the rapid low-energy decrease of spectra in Fig.4b, 4c, 4d is due to this constraint.

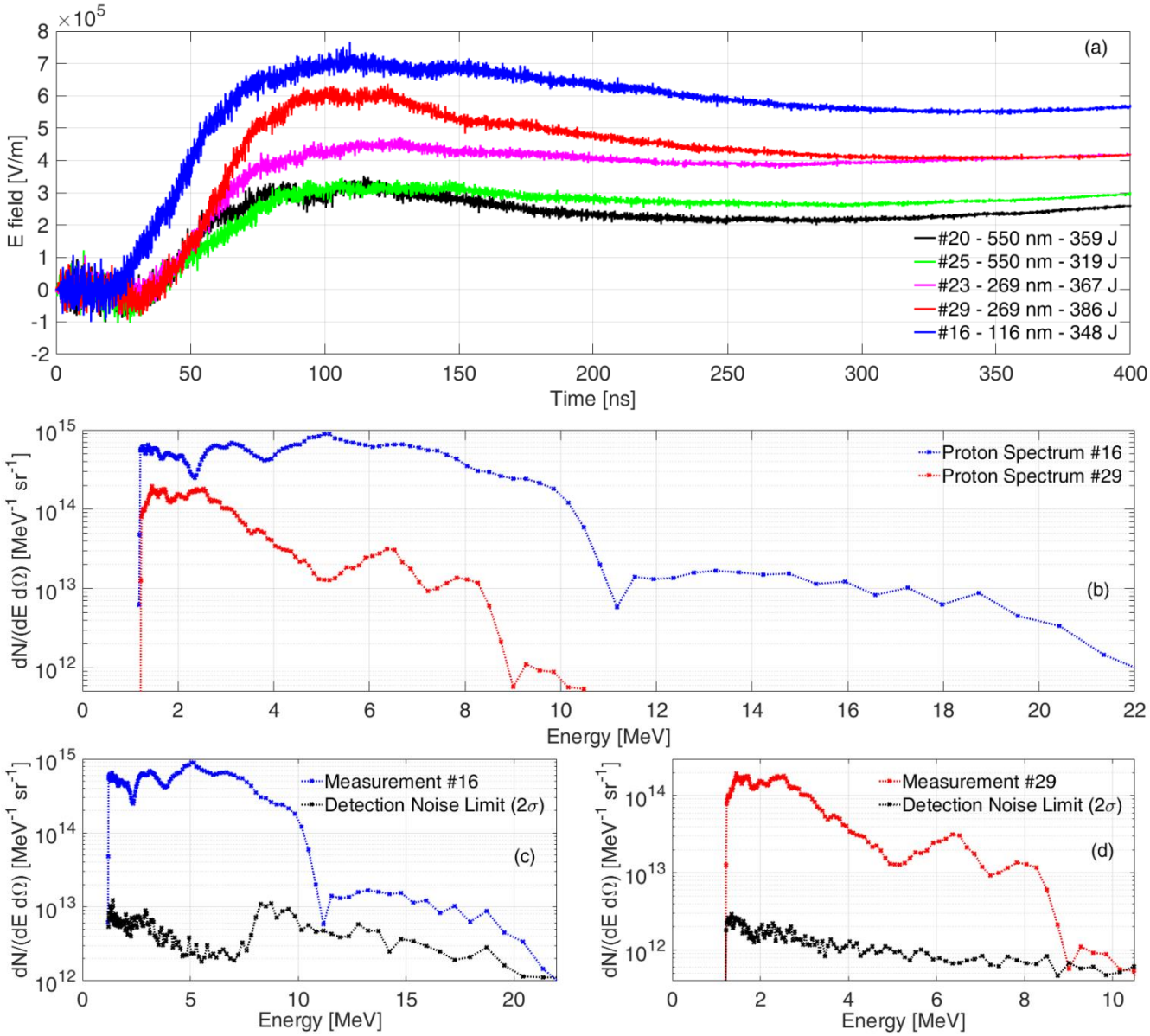

Figure 4. a) Comparison of several-shot measurements for the electrical field component normal to the D-Dot ground plane; b) spectra of the detected proton flux measured by Thomson Spectrometer TS1 for different shots. Comparison of data and Detection Noise Limit for: c) #16, with target of 116 nm thickness (see Table 1) and d) #29, with target of 269 nm thickness.

Particle-In-Cell Simulations. To have a better description of the electromagnetic field development due to charged particle dynamics in the setup used in our measurements, we performed proof-of-principle numerical simulations by means of a 3D Particle-In-Cell (PIC) code coupled with a full-wave electromagnetic solver, with details described in the Methods section. The simplified scheme is shown

in Figure 5a-5b, where the emission point is indicated by the origin of the *xyz* reference system, the same coordinate as used in Figure 1. The parabola is modelled as a thin silver layer on a thick glass cylinder, mounted on a stainless-steel annular holder. The tilted stainless-steel trapezoidal object on the right represents a section of the vacuum chamber wall close to the parabola, numerically grounded and conductively connected with the emission point on the front surface. It is well known that different ion species and electron contributions are emitted by plasmas in this regime of laser-target interaction, but for these simple and preliminary calculations we considered a very basic model, consisting of only one electron and one proton component. Emission was uniformly distributed within a $\theta = 20^{o}$ angle to target normal, and also uniform within the particle kinetic range $\left[\left(1-\frac{S}{2}\right)\beta_0;\ \left(1+\frac{S}{2}\right)\beta_0\right]$, where $\beta_0 = v_0/c$ is normalized particle velocity, with c the speed of light in vacuum and $S = \Delta\beta_0/\beta_0$ the associated velocity spread. The optimization process led to the determination of the following parameters for the two species:

- protons: $\beta_0 = 0.058$, $S = 60\% \rightarrow$ [0.774, 2.68] MeV energy; total pulse charge: 35 nC;
- electrons: $\beta_0 = 0.27$, $S = 60\% \rightarrow$ [9.40, 34.7] keV; total pulse charge: 7.5 nC.

We show in Figure 5c the comparison of the normalized electric field measured for shot #29 by the D-Dot with those obtained via numerical simulations at the same position. In particular, we show both the *x* and *u* (the sensitive D-Dot axis normal to its ground plane) components of the calculated electric field. Even with this rather simple modeling, a close agreement was reached. Note that in this picture the time origin is the moment of laser-target interaction, and the #29 measurement was thus time-shifted, with respect to Figure 3b and 4a, of the $t_s = d_{DDOT} / c$ quantity, being d_{DDOT} the D-Dot distance from origin. We find that the optimized proton kinetic energy range is in rather good correspondence with the most intense part of spectrum measured experimentally by the Thomson spectrometer for #29 and shown in Figure 4b.

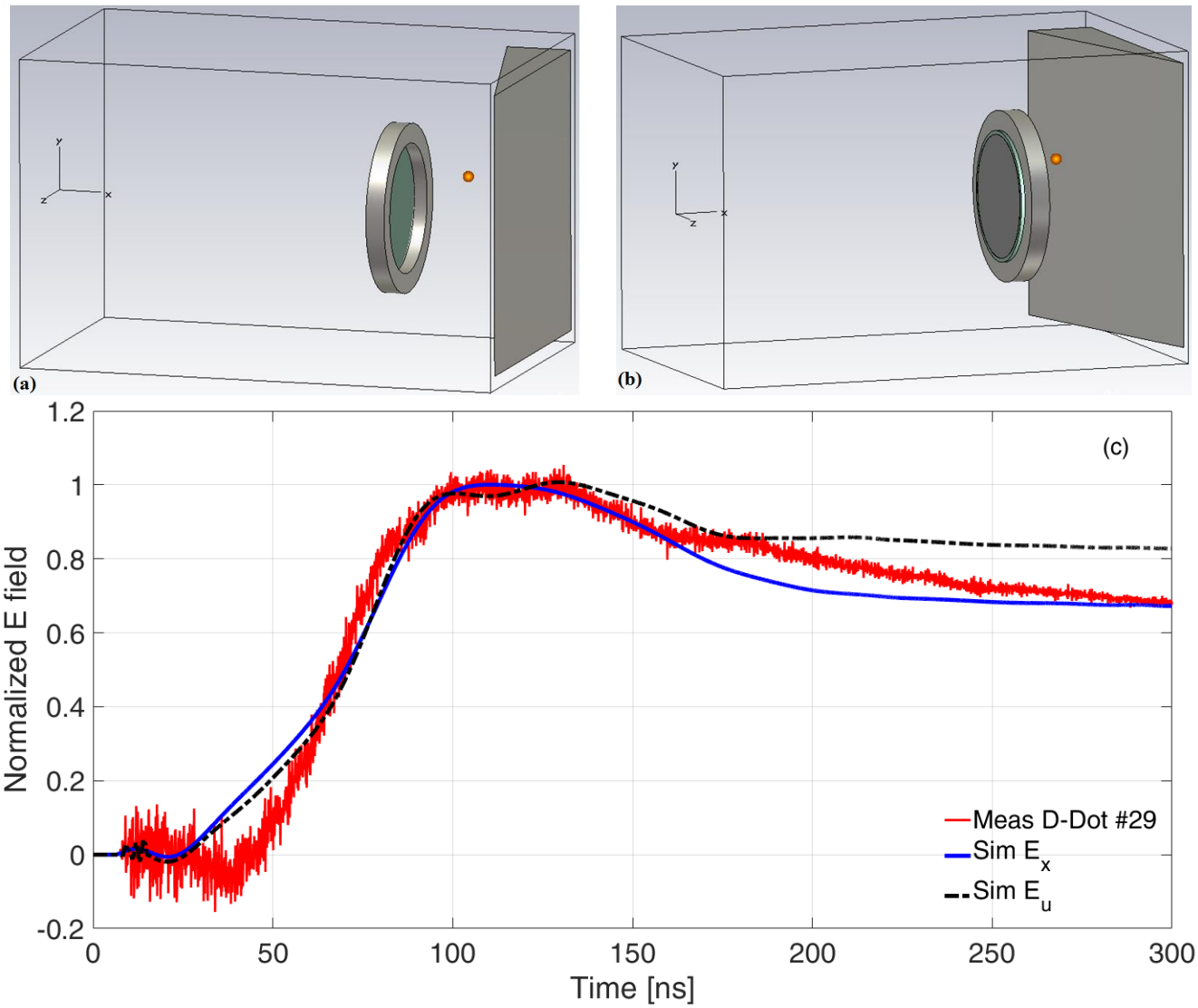

Figure 5. Geometric scheme of the model: a) and b); on both pictures the D-Dot position is indicated by the orange sphere. C) comparison between experimental D-Dot measurements from shot #29 and PIC simulations of E fields at the D-Dot position, in the $\hat{x}$ and $\hat{u}$ directions.

Calculated particle and electric-field dynamics in time are shown in Figure 6; in particular, the E_x component is displayed on the *xy* plane. After the emission, the ion bunch is accompanied and surrounded by a cloud of electrons having similar velocity (Figure 6a). Only those electrons with higher energy are capable of escaping the proton attraction and arrive at the parabola before the main charge bunch (Figure 6b). The primary increase of the electric field at the D-Dot position is principally due to the proton bunch approaching the parabola, whose effect on simulations is observed to be

important for t > 30-40 ns (Figure 6c-6d). The aforementioned fast electron component is responsible for the later rise of the field behind the mirror, which otherwise would be gradually increasing and observable from the moment of ion emission from target.

When energetic particles reach the parabola surface, secondary electrons are emitted[56]. According to the Furman model for silver[57], on a neutral surface the δ yield of secondary emitted electrons is higher than one for incoming electrons with energy in the [20,5000] eV range, reaching the mirror for t approximately in the [45, 680] ns interval. At earlier time electrons with higher energy, and thus with $\delta < 1$, are deposited on the mirror surface. A negative charged layer is thus generated from the secondary δ electrons, typically of low energy (eV level), in proximity to the associated emitting surface. The negative net charge effectively deposited on the mirror surface is thus lower than the incoming one. The actual number of secondary electrons emitted in a given time instant is also dependent on this effective net charge. For increasing time, exceeding 45 ns, δ mainly starts to become larger than one and there are thus more emitted secondary electrons than incident ones (Figure 6d-6e-6f). The accumulated negative charge on the parabola therefore starts to decrease, eventually becoming inverted in sign. At $t \sim 76$ ns the proton beam, accompanied by the low-energy electrons, begins to interact with the mirror and gives an overall positive charge to it (Figure 6d). Secondary electron emission due to incoming protons is much lower than that for electrons, because of their quite different mass and energy[56]. Particles deposited on the parabolic mirror induce a charge also on the trapezoidal section of the chamber shown in Figure 5, and the parabola and adjacent chamber section then act as a classical capacitor.

In our modeling, the electric field in the D-Dot region increases with time, and reaches a maximum at around 100 ns. For longer times, it appears to be quite stable because of the substantial charge deposited on the parabola (Figure 6e-6f). As suggested by the low slope of the measured temporal profile of the E field for longer times, the slow neutralization of the residual charge on the

parabola would finally cancel the field, and this should take place because of other particles coming at later times and charge relaxation-process through the parabola structure and holder. The fine details of the actual field-intensity distribution on the back side of the parabola will be influenced by its real-world structure, which is not modeled here in detail due to the proof-of-principle nature of these simulations, but this can be performed more accurately in future works. From simulations, the normalized time behaviour of the field in this region turns out to be rather uniform with respect to the position.

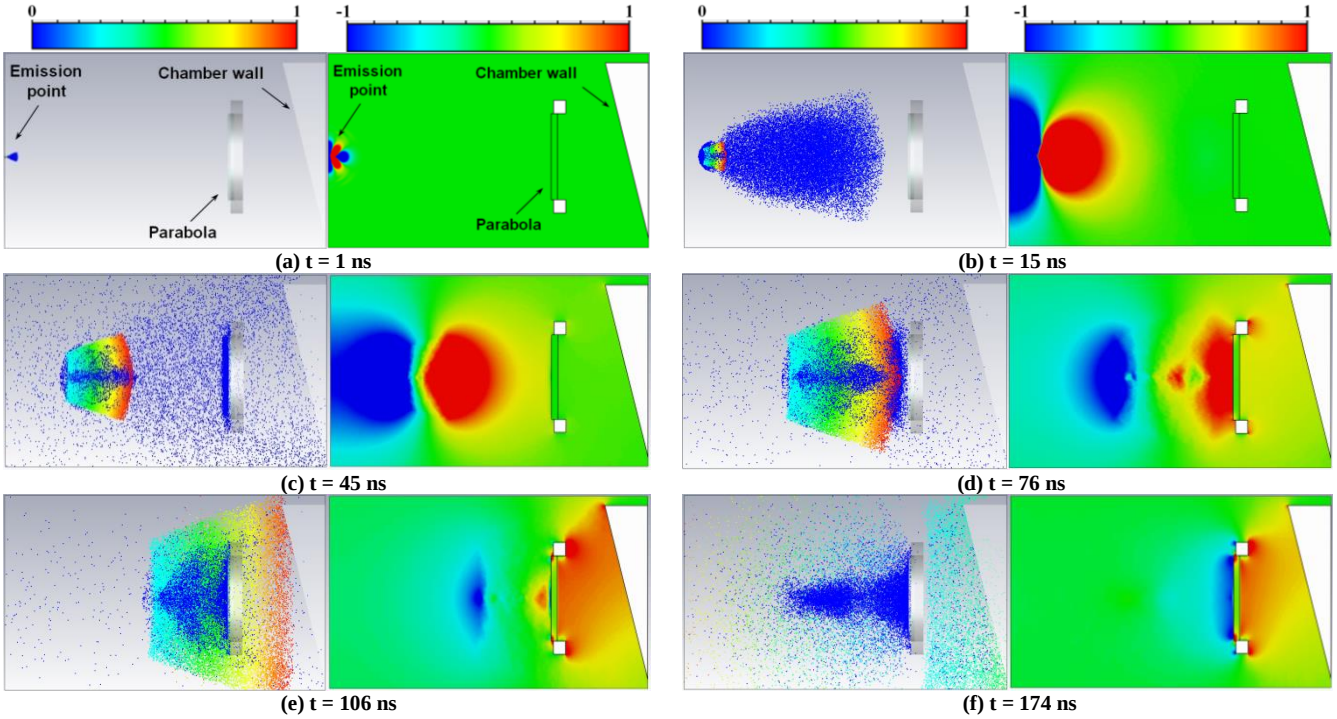

Figure 6. For each time instant, the picture on the left is the top view of particle distribution, and the adjacent one is the E_x field component on the *xy* plane. Particle energy is indicated by the colour scale, according to the normalized scale on the top of the column. Electrons are shown with deep blue colour. A normalized scale is used for the E_x intensity; it is indicated on the top of the column of each picture. The set of parabolic mirror and annular holder has a maximum transversal extension of 900 mm and is 1800 mm far from the emission point.

Discussion

The remarkably large electric-fields peaks in the MV/m range measured by the D-Dot probe, delayed with respect to the time of laser interaction, are clearly associated with charged particle dynamics, and measurements of spectra for the emitted protons in the backward direction by Thomson Spectrometer TS1 gives a clear confirmation of this point. The charge up dynamics of the parabolic mirror plus chamber-wall capacitor is indeed very well matched by simple PIC modeling with just one proton and one electron component. This approach is capable of giving good agreement with the measured evolution of electric fields and supplies useful information on their development and distribution in space and time during the parabola-mirror charging process. Of course, more accurate simulations can be performed in future from more detailed modeling of the physical structure, but this lies outside the scope of the work presented here.

In experiments of this type, an intense burst of UV, X and γ emission is produced at the moment of laser-target interaction, together with the creation of beams of relativistic electrons. The electromagnetic contribution is capable of generating photoionization on any exposed surface, and thus creates a layer of emitted electrons with ~eV energy surrounding it, leaving a transient superficial positive charge. On a slightly longer timescale, relativistic electrons are expected to deposit a negative charge on the same surfaces, since secondary electron emission at those energies is much smaller than unity[57,58]. It is currently under investigation, and definitely not trivial, to estimate what the net effect due to the superimposition of these two processes is, in terms of possible associated electric fields. As a matter of fact, these should be detectable during the early moments of the measurements performed by our D-Dot probe (Fig.3c,4a,5c), but the contemporary presence on the same detector of the 172 kV/m peak field value of the *high-frequency component* due to classical EMP, might hide them.

According to previously documented experimental campaigns[32], the type of experiments we have reported here – several hundred joules, ps laser pulse, intensity higher than 10^{20} W/cm^2 - is

expected to generate the highest values of EMP fields, here identified with the HFC of measured signals, which have one well-recognized generation mechanism due to target charging because of electron emission and the subsequent neutralization current flowing through the target holder[28,29,32]. Indeed, in this work we have shown that, depending on the position within the experimental chamber, LFC fields due to deposited charges can be approximately four times higher than EMP fields created by the primary target. In laser-matter interaction experiments, it is very common to use films or slabs for filtering or completely shielding objects from radiation coming from plasma. As demonstrated here, the deposition of emitted charge on the same filters and shields can induce a very high quasi-electrostatic field, which will be applied to those same objects thought to be protected, and thus might cause severe damaging to their electronics. This is a subtle issue, and is one that should be carefully taken into account when the use of filters and shields is necessary in these contexts. However, these considerations are generally applicable to any region and structure within the chamber, since charge can be deposited on each surface directly exposed to plasma. This is an important result, because such huge fields can be very detrimental for the operation of all the electronic equipment in laser-matter experiments. For this reason the investigation of intense electromagnetic fields is now of great importance and currently a hot topic for present and future plants for laser-plasma acceleration (*PETAL*[58], *ELI*[59,60], *Apollon*[61]) and for inertial-confinement-fusion (*NIF*[44,45,62], *LMJ*[58]).

We have described here, for the first time, sources and evolution in time and space of the large electric fields associated with the charging process of a capacitor-collector structure, due to the large flux of particles emitted and accelerated by powerful laser interaction with matter. This opens up the study of more complex structures, where different electric-field distributions can be achieved remote from the initial laser-plasma interaction. The electrical field in a classical parallel-plate capacitor scales with the q/S ratio (being q the total deposited charge and S the plate surface). If, for instance, a set of open capacitors is connected in series (see Figure 7), it is possible to deposit the laser-driven charge

only on one surface of the first capacitor - acting as an effective charge collector - and then easily create several consecutive regions where the field E_i is differently scaled according to the local plate-surface S_i, with i capacitor index. In case of a very small associated surface, giant electric fields might be obtained. To make a simple estimation, we can consider to use the 620 mm mirror plate as charge collector, in case of the associated field profiles of several hundreds of kV/m described in Figure 4a. Thus, in a hypothetical following series capacitor with an electrode having just 20 mm diameter we might easily reach the order of several hundreds of MV/m electric fields. Several tens of GV/m fields might be also obtained for an electrode of 1 mm diameter. Obviously, the actual limit to the field intensity is given by the breakdown induced in vacuum, which is strictly related to the electrode material, geometry, roughness, conditioning and also to the type and the pressure of the residual gas. However this breakdown also takes a finite time to develop and begin to neutralize the electric field, holding out the potential for the practical use of these extreme MV/m to GV/m fields over short timescales. Of course, these structures can also be readily designed to obtain non-spatially-uniform field distributions tailored for specific applications, e.g. for control of a laser acceleration ion bunch.

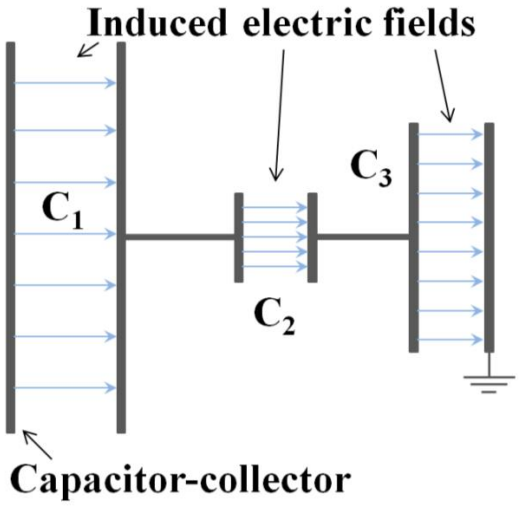

Figure 7. Series connection, to the capacitor-collector, of further capacitors with plates of different surface S_i, and associated different E_i fields.

In summary, the conclusion of our work is that these high fields can be generated in regions well-shielded against ionizing radiation coming from a laser-matter interaction, that their measurement can be easily and accurately performed by classical conductive field-probes, that the scheme of charge deposition and field generation is versatile, allows for the definition of complex field distributions, and can be efficiently employed with repetitive powerful lasers, for example running at 10 Hz. These electric fields can be used for deflection and energy-selection, in an electron-spectrometer-like configuration[34], of the particle beams emitted by a separate conventional accelerator or one based on laser-plasma interactions. Focusing may also be achieved if charge is conveyed to a classical electrostatic lens[34]. The separation of the two stages - acceleration and conditioning of the beam - is potentially very helpful for the independent optimization of each process, with respect to examples such as those proposed by references[3,7,9]: a large charge might be deposited on the capacitor for effective focusing, regardless of the details of the accelerated bunch. This permits high electric fields and related voltages to be achieved, with short (few picosecond) rise-time and at desired time instant, which is very difficult to be obtained with conventional power supplies. This configuration is much more compact and effective for electric beam-conditioning purposes. Once charge is accumulated on the collector, a delayed second laser can be used to trigger a fast photo-conductively activated spark-gap switch[63,64], short-circuiting the accumulated charge to ground and thus generating very high currents. The technology of these powerful devices allows them to support several tens of kA currents and up to MV voltages with rise times and jitters lower than 100 ps[63-65]. For a reasonable stored charge in the μC range[1,29,32] peak currents of the order of tens of kA, very well synchronized with the second laser, may be achieved. This is the range of currents required in a helical-coil structure[9] to drive an ultrashort travelling electromagnetic pulse, demonstrated to be very effective for controlling and optimizing up to MeV laser-accelerated ions. Moreover, very high magnetic fields can be generated

with these pulsed currents[20-23,27,33], which can be effectively used again for particle beam conditioning[4,5,8], and also for studies of plasma physics, material science, atomic and molecular physics[20,21] and laboratory experiments of astrophysical interest[16,33].

The demonstrated generation of such temporally and spatially controlled fields of high intensity and wide distribution opens up possibilities for the new and significant employment of laser-plasma interaction for *powerful and versatile field sources*, of direct interest not only to particle-acceleration schemes, for which is indeed of primary importance, but also to a multidisciplinary range of applications in different scenarios. To name a few examples, they can be tailored to and very advantageous for biological and medical studies of interactions with cells[35], material and device characterization[36-39], EMP-radiation-hardening of components and electromagnetic compatibility studies[38,39], and terahertz radiation coming from laser-created plasmas[40,41].

Methods

Experiment description. Experiments were performed using the Vulcan Petawatt laser at the Rutherforth Appleton Laboratory operating at its fundamental wavelength of 1054 nm, for pulses of ~1 ps duration and focused intensity in target beyond 10^{20} W/cm^2, as summarized in Table 1. The contrast was > 10^{10} on a nanosecond timescale and > 10^6 at 200 ps before of main pulse. The thickness of the Parylene-N foil targets used (1.1 g/cm^3 mass density) is also given in the table.

Table 1. Shots parameters. No measurement of pulse duration were obtained for #23, where the focal spot area was of the order of $4 \cdot 10^{-7}$ cm^2. For a reasonable pulse width in the [980,1700] fs interval, we can estimate a peak intensity in the $[5.4,9.4] \cdot 10^{20}$ W/cm^2 range.

#	Target Thickness [nm]	Energy [J]	Duration [fs]	Intensity [10^{20} W/cm^2]
20	550	359	980	14.3
25	550	319	1000	10.9
23	269	367	-	-
29	269	386	1700	4.8
16	116	348	1220	10.8

Electric field probe. A customized version of the AD-80D(R) D-Dot differential electric field sensor[42] (3 dB bandwidth up to 5.5 GHz) was placed behind the parabola mirror (see Figure 2). It was positioned at the (2193 mm, 150 mm, -196 mm) coordinates, for d_{DDOT} = 2207 mm overall distance from origin, with its sensitive direction (normal to its ground plane): $\hat{u} = 0.12\hat{x} + 0.87\hat{y} + 0.49\hat{z}$. The position and orientation were set for efficient protection against initial direct ionizing radiation due to the laser-matter interaction. The BIB-100G balun (250 KHz – 10 GHz bandwidth) was connected to its terminals. A double-shielded RG402 cable ~25 m long connected it to a 12.5 GHz Tektronix DPO71254C oscilloscope, which was used at 50 GS/s acquisition rate on a single channel, leading to an effective 3 dB bandwidth of ~6 GHz. The cable-connection was characterized off-line by means of a Vector Network Analyzer Agilent N5230A (10 MHz - 20 GHz), and its complex transfer function ($A_C(f)$) was determined. Therefore, from the V_{DDOT} signal measured on the scope, it was possible to accurately deconvolve that at the balun output:

$$V_{DDOT-B}(t) = \mathcal{F}^{-1}\{A_C^{-1}(f) \cdot \mathcal{F}\{V_{DDOT}(t)\}(f)\}(t), \quad (1)$$

where $\mathcal{F}$ and $\mathcal{F}^{-1}$ are the Fourier Transform and Inverse Fourier Transform operators, respectively. The component of the applied electric-field normal to the D-Dot ground plane was recovered by time integration[43]:

$$E_n(t) = K_{DDOT-B} \int_0^t V_{DDOT-B}(\tau) d\tau, \quad (2)$$

being $K_{DDOT-B} = 9.5 \cdot 10^{12}$ $m^{-1}s^{-1}$ a characteristic constant which comprises also the Balun attenuation.

It is well known that the accurate detection of electromagnetic fields by conductive probes is a very delicate and challenging task in experiments with energetic picosecond lasers[33,45,66,67], especially when the probe is placed inside the experimental chamber. For this reason, considerable care was taken

with cable shielding and the scope was placed around 15 m far from the vacuum chamber, to suppress direct EMP coupling to it. Possible currents induced on the external conductor of the double-shielded coaxial cables were effectively suppressed by the application, around the cables, of a tailored series of toroids of different materials. We also used a second identical cable not coupled to a probe for background estimation. This followed the same path of that connected to the balun, was terminated with a 50 ohm load on the vacuum side and connected to another scope channel; thus we verified that any possible coupling, if present, was much lower than the noise level on that channel for those acquisitions.

Measurement accuracy. Oscilloscope resolution and sensitivity limit the minimum value of measured V_{DDOT}, and as a direct consequence the accuracy of E_n that we can obtain from equation (2). In Figure 3a the acquisition has a time duration much larger than the actual measured signal, and as a matter of fact for $t > 600$ ns we obtained a useful measurement of the scope *background noise*. From the accurate analysis of this time interval, and comparison with acquisitions on null shots where the laser did not actually hit the target, it was possible to estimate the uncertainty on the two components (LFC and HFC) of the reconstructed electric field. In particular, for the LFC field intensity is $N_{LFC\text{-}FIELD}$ ~20 kV/m, and for the associated field slope $N_{LFC\text{-}SLOPE}$ ~ 370 V m^{-1}ns^{-1}. This slope uncertainty is equivalent to a lower observable frequency ~1 MHz. This is clearly not an issue for the HFC, and its intensity uncertainty was estimated: $N_{HFC\text{-}FIELD}$ ~ 10 kV/m peak-to-peak. In Table 2, the values of the average slopes on the different time-intervals of signal in Figure 3c are supplied and compared with the related $N_{LFC\text{-}SLOPE}$.

Table 2. Average slope for all the intervals for the reconstructed electric field of Figure 3c and comparison with $N_{LFC\text{-}SLOPE}$.

Interval	Time interval [ns]	|Average slope| [V m^{-1} ns^{-1}]	|Average slope|/ $N_{LFC\text{-}SLOPE}$
a	0 - 30	992	~2.7
b	30 - 93	10011	~27
c	93 - 125	74	~0.2
d	125 - 167	1987	~5.3
e	167 - 266	895	~2.4
f	266 - 599	66	~0.2

We find a very good reconstruction of the original signal slope, with respect to 'noise', in the *b* and *d* time intervals show in Figure 3; there is still some reasonable signal-to-noise ratio in the *e* interval. Poor accuracy was obtained in intervals *c* and *f* because of the small slope, and also in the *a* interval, but in this case because the amplitude was only 1.5 times higher than $N_{LFC\text{-}FIELD}$ (Figure 3b).

Thomson Spectrometer. The Thomson Spectrometer TS1 was placed 39 cm from the foil target, at an angle of 69^{o} with respect to $\hat{x}$. Magnetic deflection was performed over a 50 mm length, with an applied maximum magnetic field of 0.54 T. Electrostatic deflection was achieved in a tapered-electrode structure of similar height with a plate length of 200 mm, minimum and maximum plate separation of 2.5 mm and 20 mm, respectively, for an applied potential difference of 6250 V. Imaging Plate BAS-TR was employed as an ion detector, and associated calibration data for protons[68,69] was used to obtain the spectra shown in Figure 4. For the estimation of the detection noise-level, a section of the imaging plate was taken as close as possible to the proton parabola line, and from it the associated noise level σ was obtained. An arbitrary detection level of 2σ is here considered for suitable data accuracy, and shown for shots #16 and #29 in Figure 4c-4d. The lower energy-threshold of ~1 MeV observed in Fig. 4b, 4c, 4d is due to the geometrical constraints of the spectrometer.

PIC Simulations. Simulations were performed by the commercial code CST Particle Studio®. Its particle-in-cell solver can perform fully-consistent simulations of particles and electromagnetic fields

in the time domain. Fields are calculated by the Finite Integration Technique[70] which is applied to the integral form of Maxwell's equations in time domain. The focusing parabola is placed 1800 mm from the emission point, and modelled as a thin silver layer of 620 mm diameter on a 110 mm thick glass cylinder of 650 mm diameter, mounted on a 100 mm-thick stainless-steel annular holder with a 900 mm external diameter. The precise detail of the structure of the back side of the parabola is important for the determination of the actual electric fields. The presence of sharp corners or surfaces may greatly increase the local electric field distribution for a given deposited charge. In these proof-of-principle simulations we deal with the phenomenological modeling of the parabola charging, so a simple geometric scheme was considered. More detailed designs can be prepared for future more accurate studies. Space-charge effects were computed, together with secondary electron emission[57] and superficial charge deposition on all the surfaces. Here we are not interested in the acceleration process during the laser-matter interaction, but rather in the fields associated with particles when they are rather far from the emission zone. This allows for the use of more relaxed conditions in simulations. Particles were modeled with a Gaussian time-profile $A\, e^{-\frac{t^2}{2\tau^2}}$, having maximum emission at the initial time of the simulation t = 0, with a τ = 0.5 ns inflection point with respect to the maximum. The bunch time-dependence is slightly modified from the classical Gaussian as to be zero at t = 1 ns. We kept the overall bunch charge to low values to minimize space-charge effects, causing excessive enlargement of the actual beam divergence with respect to the 20^o setting, and thus mainly leading to fewer particles intercepting the far parabolic mirror. The emission point is modelled as a circular surface of 1 mm radius on the *yz* plane, divided into with 1521 sub-surfaces of equal emission properties. The actual time step used for stable and accurate simulation in our case was 4.75 ps. The simulation box dimensions were 2667 mm, 1653 mm and 1557 mm along *x*, *y* and *z* axes, respectively. A maximum frequency of 1 GHz was set for the algorithm of λ-based adaptive mesh refinement. Twenty lines per

wavelength are used as a general indication, and the local mesh distance is changed according to the shape and local dimension of modelled objects, for a total number of about $7.5 \cdot 10^6$ mesh cells. Minimum and maximum mesh step sizes were 1 mm and 17.05 mm, respectively.

As shown in Figure 5c, these simulations produced results which are in rather fine agreement with normalized laboratory measurements. This simple model is less appropriate if we seek to reproduce the actual maximum field of the measurements. In this case it is necessary to describe also the acceleration process and to find the correct tailored proportion of multiple electron and ion populations from the moment of emission[1]. Moreover, as previously mentioned the field is not only due to deposited charge but also influenced by the precise conformation of the setup we used in the vacuum chamber, and especially by the back side of the parabola and its mounting hardware. For all of these reasons, the multi-scale extensive simulations required to reproduce the actual field intensity are definitely not an easy task, and can be considered for later evolutions of this work.

References

[1] Macchi, A., Borghesi, M., Passoni, M. Ion acceleration by superintense laser-plasma interaction. *Rev. Mod. Phys.* **85**, 751 (2013).

[2] Toncian, T. *et al*. Ultrafast laser–driven microlens to focus and energy-select mega–electron volt protons. *Science* **312**, 410 (2006).

[3] Kar, S. *et al*. Dynamic control of laser-produced proton beams. *Phys. Rev. Lett.* **100**, 105004 (2008).

[4] Ter-Avetisyan, S., Schnürer, M., Polster, R., Nickles, P.V., Sandner, W. First demonstration of collimation and monochromatisation of a laser accelerated proton burst. *Laser Part. Beams* **26**, 637 (2008)

[5] Schollmeier, M. *et al*. Controlled transport and focusing of laser-accelerated protons with miniature magnetic devices. *Phys. Rev. Lett.* **101,** 055004 (2008).

[6] Toncian, T. *et al*. Properties of a plasma-based laser-triggered micro-lens, *AIP Adv.* **1**, 022142 (2011).

[7] Bartal, T. *et al*. Focusing of short-pulse high-intensity laser-accelerated proton beams. *Nat. Phys.* **8**, 139 (2012).

[8] Busold, S. *et al*. Focusing and transport of high-intensity multi-MeV proton bunches from a compact laser-driven source. *Phys. Rev. Spec. Top.-Accel. Beams* **16**, 101302 (2013).

[9] Kar, S. *et al.* Guided post-acceleration of laser-driven ions by a miniature modular structure. *Nat. Comm.* **7**, 10792 (2016).

[10] Mackinnon, A. J. *et al*. Proton radiography of a laser-driven implosion. *Phys. Rev. Lett.* **97**, 045001 (2006).

[11] Borghesi, M. *et al*. Laser-driven proton acceleration: source optimization and radiographic applications. *Plasma Phys. Control. Fusion* **50**, 124040 (2008).

[12] Bulanov, S. V., Esirkepov, T. Zh., Khoroshkov, V. S., Kuznetsov, A. V., Pegoraro, F. Oncological hadrontherapy with laser ion accelerators. *Phys. Lett. A* **299**, 240 (2002).

[13] Yogo, A. *et al*. Measurement of relative biological effectiveness of protons in human cancer cells using a laser-driven quasimonoenergetic proton beamline. *Appl. Phys. Lett.* **98**, 053701 (2011)

[14] Fritzier, S. *et al*. Proton beams generated with high-intensity lasers: applications to medical isotope production. *Appl. Phys. Lett.* **83**, 3039 (2003).

[15] Remington, B. A., Arnet, D., Drake, R. P., Takabe, H. Modeling astrophysical phenomena in the laboratory with intense lasers. *Science* **284**, 1488 (1999).

[16] Albertazzi, B. *et al*. Laboratory formation of a scaled protostellar jet by coaligned poloidal magnetic field. *Science* **346,** 325 (2014).

[17] Dyer, G. M. *et al*. Equation of state measurements of dense plasma heated with fast protons. *Phys. Rev. Lett.* **101**, 015002 (2008).

[18] Higginson, D. P. *et al*. Laser generated neutron source for neutron resonance spectroscopy. *Phys. Plasmas* **17**, 100701 (2010).

[19] Atzeni, S., Meyer-ter-Vehn, J. *The Physics of Inertial Fusion: Beam Plasma Interaction, Hydrodynamics, Hot Dense Matter* (Oxford University Press, 2009)

[20] Fujioka, S. *et al*. Kilotesla magnetic field due to a capacitor-coil target driven by high power laser. *Sci. Rep.* **3,** 1170 (2012).

[21] Santos, J. J. *et al*. Laser-driven platform for generation and characterization of strong quasi-static magnetic fields. *New J. Phys.* **17**, 083051 (2015).

[22] Law, K. F. F. *et al*. Direct measurements of kilo-tesla level magnetic field generated with laser-driven capacitor-coil target by proton deflectometry. *Appl. Phys. Lett.* **108**, 091104 (2016).

[23] Tikhonchuk, V.T., Bally-Grandvaux, M., and Santos J. J. Quasistationary magnetic field generation with a laser-driven capacitor-coil assembly. *Phys. Rev. E* **96**, 023202 (2017).

[24] Korneev, P., d'Humières, E., Tikhonchuk, V. Gigagauss-scale quasistatic magnetic field generation in a snail-shaped target. *Phys. Rev. E* **91**, 043107 (2015).

[25] Kruer, W.L. *The Physics of Laser Plasma Interactions* (Westview Press, 2003).

[26] Gibbon, P. *Short Pulse Laser Interactions With Matter* (Imperial College Press, 2005).

[27] Daido, H. *et al.* Generation of a strong magnetic field by an intense co2 laser pulse. *Phys. Rev. Lett.* **56**, 846 (1986).

[28] Dubois, J.-L. *et al.* Target charging in short-pulse-laser–plasma experiments. *Phys. Rev. E* **89**, 013102 (2014).

[29] Poyé, A. *et al*. Dynamic model of target charging by short laser pulse interactions. *Phys. Rev. E* **92**, 043107 (2015).

[30] Quinn. K. *et al*. Laser-driven ultrafast field propagation on solid surfaces. *Phys. Rev. Lett.* **102,** 194801 (2009)

[31] Tokita, S., Sakabe, S., Nagashima, T., Hashida, M., Inoue, S. Strong sub-terahertz surface waves generated on a metal wire by high-intensity laser pulses. *Sci. Rep.* **5,** 8268 (2015).

[32] Poyé, A. *et al*. Physics of giant electromagnetic pulse generation in short-pulse laser experiments. *Phys. Rev. E* **91**, 043106 (2015).

[33] Albertazzi, B. *et al*. Production of large volume, strongly magnetized laser-produced plasmas by use of pulsed external magnetic fields. *Rev. Sci. Instrum.* **84**, 043505 (2013)

[34] Szilagyi, M. *Electron and ion optics* (Plenum Press, 1988).

[35] Pakhomov, A.G., Miklavčič D., Markov M.S., edts. *Advanced electroporation techniques in biology and medicine* (CRC Press, 2017)

[36] Gupta, K. M., Gupta, N. *Advanced electrical and electronics materials: processes and applications.* (Wiley, 2015)

[37] Nalwa, H. S., edt. *Handbook of low and high dielectric constant materials and their applications*. (Academic Press, 1999)

[38] Ott, H. W. *Electromagnetic compatibility engineering.* (John Wiley & Sons, 2009)

[39] Christopoulos C. *Principles and techniques of electromagnetic compatibility* (CRC Press, 2007)

[40] Houard, A., Liu, Y., Prade, B., Tikhonchuk, V. T. & Mysyrowicz, A. Strong Enhancement of Terahertz Radiation from Laser Filaments in Air by a Static Electric Field. *Phys. Rev. Lett.* **100**, 255006 (2008).

[41] Singh, R. K., Kumar, S. & Sharma R.P. Generation of electromagnetic waves in the terahertz frequency range by optical rectification of a Gaussian laser pulse in a plasma in presence of an externally applied static electric field. *Contrib. Plasma Phys.* **57**, 252 (2017).

[42] Edgel, W.R. *Primer on electromagnetic field measurements, Prodyn Application note, PAN 895, 1-14.* (Date of access: 18/10/2017) Available at http://ppmtest.com/wp-content/uploads/ap895-primer-on-electromagnetic-field-measurements.pdf.

[43] Mead, M.J., Neely, D., Gauoin, J., Heathcote, R. & Patel, P. Electromagnetic pulse generation within a petawatt laser target chamber. *Rev. Sci. Instrum.* **75**, 4225-4227 (2004).

[44] Brown Jr., C.G. *et al*. Assessment and mitigation of electromagnetic pulse (EMP) impacts at short-pulse laser facilities. *J. Phys.: Conf. Ser.* **244,** 032001 (2010).

[45] Brown Jr., C.G. *et al*. Assessment and mitigation of diagnostic-generated electromagnetic interference at the National Ignition Facility. *Rev. Sci. Instrum.* **83**, 10D729 (2012);

[46] Consoli, F., De Angelis, R., Andreoli, P., Cristofari, G. & Di Giorgio, G. Measurement of the radiofrequency-microwave pulse produced in experiments of laser-plasma interaction in the ABC laser facility. *Phys. Procedia* **62**, 11-17 (2015).

[47] Consoli, F. *et al*. Experiments on electromagnetic pulse (EMP) generated by laser-plasma interaction in nanosecond regime, *in Proceedings of the IEEE 15th International Conference on Environment and Electrical Engineering (EEEIC), Rome, June 2015, edited by L. Martirano, R. Araneo, Z. Leonowicz, M.C. Falvo, 182-187*, ISBN 978-1-4799-7993-6/, doi 10.1109/EEEIC.2015.7165537. (2015).

[48] De Marco, M. *et al*. Basic features of electromagnetic pulse generated in a laser-target chamber at 3-TW laser facility PALS, *J. Phys.: Conf. Ser.* **508,** 012007 (2014).

[49] Krása, J., *et al.* Spectral and temporal characteristics of target current and electromagnetic pulse induced by nanosecond laser ablation. *Plasma Phys. Control. Fusion* **59**, 065007 (2017).

[50] Cikhardt, J. *et al*. Measurement of the target current by inductive probe during laser interaction on terawatt laser system PALS. *Rev. Sci. Instrum.* **85**, 103507 (2014).

[51] Ceccotti, T., *et al*, Proton acceleration with high-intensity ultrahigh-contrast laser pulses. *Phys. Rev. Lett*. **99**, 185002 (2007)

[52] Prasad, R., *et al*. Fast ion acceleration from thin foils irradiated by ultra-high intensity, ultra-high contrast laser pulses. *Appl. Phys. Lett.* **99**, 121504 (2011).

[53] McKenna, P., *et al.* Characterization of proton and heavier ion acceleration in ultrahigh-intensity laser interactions with heated target foils, *Phys. Rev. E* **70**, 036405 (2004)

[54] Fuchs, J., *et al*. Comparison of laser ion acceleration from the front and rear surfaces of thin foils. *Phys. Rev. Lett.* **94**, 045004 (2005)

[55] Fuchs, J., *et al*. Comparative spectra and efficiencies of ions laser-accelerated forward from the front and rear surfaces of thin solid foils. *Phys. Plasmas* **14**, 053105 (2007).

[56] Bruining, H. *Physics and applications of secondary electron emission, 2nd Edition* (Pergamon Press, 1962).

[57] Furman, M. A. & Pivi, M. T. F. Probabilistic model for the simulation of secondary electron emission. *Phys. Rev. ST Accel. Beams* **5**, 124404 (2002).

[58] Casner, A. *et al.* LMJ/PETAL laser facility: overview and opportunities for laboratory astrophysics. *High Energ. Dens. Phys*. **17,** 2 (2015).

[59] Mourou, G., Korn, G., Sandner, W., Collier, J. L. *ELI - Extreme Light Infrastructure: Science and Technology with Ultra-Intense Lasers, Whitebook* (THOSS Media GmbH, 2011).

[60] Le Garrec, B. *et al.* ELI-Beamlines: extreme light infrastructure science and technology with ultra-intense lasers. *Proc. SPIE* **8962,** 89620I (2014).

[61] Zou, J.P. *et al*. Design and current progress of the Apollon 10 PW project. *High Pow. Las. Sci. Engin.* **3**, e2 (2015).

[62] Eder, D. C. *et al*. Mitigation of Electromagnetic Pulse (EMP) Effects From Short-Pulse Lasers And Fusion Neutrons, Lawrence Livermore National Laboratory, Technical Report LLNL-TR-411183, (Date of access: 18/10/2017) Available at https://e-reports-ext.llnl.gov/pdf/370813.pdf. (2009).

[63] Brussaard, G. J. H., Hendriks, J. Photoconductive switching of a high-voltage spark gap. *Appl. Phys. Lett.* **86**, 081503 (2005).

[64] Hendriks, J., Broks, B. H. P., van der Mullen, J. J. A. M., Brussaard, G. J. H. Experimental investigation of an atmospheric photoconductively switched high-voltage spark gap. *J. Appl. Phys.* **98**, 043309 (2005).

[65] Schwarz, H.J., Hora H., edts. *Laser interaction and related plasma phenomena* (Plenum Press, 1971).

[66] Consoli, F. *et al*. Time-resolved absolute measurements by electro-optic effect of giant electromagnetic pulses due to laser-plasma interaction in nanosecond regime. *Sci. Rep.* **6**, 27889 (2016).

[67] Robinson, T.S. *et al*. Low-noise time-resolved optical sensing of electromagnetic pulses from petawatt laser-matter interactions. *Sci. Rep.* **7**, 983 (2017).

[68] Bonnet, T. *et al.* Response functions of Fuji imaging plates to monoenergetic protons in the energy range 0.6–3.2 MeV. *Rev. Sci. Instrum.* **84**, 013508 (2013).

[69] Mančić, A. *et al.* Absolute calibration of photostimulable image plate detectors used as (0.5 – 20 MeV) high-energy proton detectors. *Rev. Sci. Instrum.* **79**, 073301 (2008).

[70] Carstensen, C., Funken, S., Hackbusch, W., Hoppe, R. H. W., Monk P., edts. *Computational Electromagnetics* (Springer-Verlag, 2003).

Acknowledgments

The work of F.C and R.D.A. has been partially carried out within the framework of the EUROfusion Consortium and has received funding from the Euratom research and training programme 2014–2018

under grant agreement No. 633053. The views and opinions expressed herein do not necessarily reflect those of the European Commission.

Author Contributions

F.C. and R.D.A. discussed the measurements with R.A.S., the principal investigator, prior to the experiment. F.C. and R.D.A. performed the D-Dot measurements. F.C. analyzed the data of D-Dot probe and performed the PIC simulations. S.G. and G.S.H. analyzed the measurements by Thomson ion spectrometer. F.C. discussed the results with R.D.A, T.S.R, S.G. and R.A.S, prepared the figures - with the exception of Fig. 4b,4c,4d and the associated discussion, which were provided by S.G. - and wrote the manuscript, with valuable advices by R.D.A, T.S.R. and R.A.S.; S.G. was the lead researcher on the main experimental campaign studying laser interaction with optically levitated and foil targets that provided the experimental platform for the work. G.S.H., S.J.E., E.J.D. and O.C.E. were responsible for proton diagnostics. Z.N. was the principal investigator for the charged-particle related aspect of the experiment. M.N. was the facility link-scientist and was involved heavily in the planning and logistics of the experiment. All the authors participated in the five week experimental campaign, reviewed and approved the manuscript.

Additional Information

Competing financial interests: The authors declare no competing financial interests.